Computational fluid dynamics modeling of airlift VUV/UV photoreactor with internal circulation

Minghan Luo[a,b], Wenjie Xu[a], Jiaxing Xu[a], Gongde Wu[a,b], Taeseop Jeong[c,*]

[a]School of Environmental Engineering, Nanjing Institute of Technology, No. 1 Hongjing Avenue Jiangning Science Park, Nanjing, Jiangsu, PR. China, CN211167, Tel. +86 25 8611 8963; emails: leon96201@njit.edu.cn (M. Luo), wenjiexu@njit.edu.cn (W. Xu), xujiaxing1987@163.com (J. Xu)
[b]Energy Research Institute, Nanjing Institute of Technology, No. 1 Hongjing Avenue Jiangning Science Park, Nanjing, Jiangsu, PR. China, CN211167, Tel. +86 139 1299 3165; email: wugongde@njit.edu.cn
[c]Department of Environmental Engineering, Chonbuk National University, 567 Baekje-daero, Deokjin-gu, Jeonju-si, Jeollabuk-do, 54896 Republic of Korea, Tel. +82 63 270 2447; email: jeongts@jbnu.ac.kr

ABSTRACT

Ultraviolet (UV) chemical degradation is a low-cost, environmentally friendly, and sustainable wastewater treatment technology. In this study, we designed an airlift photoreactor with internal circulation and explored the effect of its flow characteristics (hydrodynamics) on the reaction to improve the degradation efficiency of pollutants in water. The continuous flow vacuum ultraviolet (VUV)/UV method was used to evaluate the degradation ability of pollutants in the reactor in terms of computational fluid dynamics (CFD), mass transfer, and photoreaction kinetic models. Results show that the turbulence intensity and circulation effect in the reactor are ideal in the range of gas flow rate used in this study, and the chance of UV radiation can be effectively improved. The formation of OH radicals and the decomposition efficiency of methylene blue (MB) in the VUV/UV process is strongly correlated with the mixing strength in the reactor. The computational results of the CFD model are close to the experimental results, but the efficiency of CFD in MB processing is higher than the experimental results. This finding is because the scavenger effect of MB decomposition by-products is not fully considered in CFD kinetic analysis.

Keywords: Vacuum ultraviolet/Ultraviolet; Photoreactor; Computational fluid dynamics; Water treatment; Methylene blue

1. Introduction

Ultraviolet advanced oxidation processes (UV AOPs) have been studied for more than 30 y. UV AOP disinfection technology has been widely used in drinking water treatment plants. The degradation of harmful pollutants in wastewater treatment shows great potential [1,2]. Therefore, the vacuum ultraviolet (VUV) process has shown broad application prospects in wastewater treatment. The VUV/UV process uses a mercury lamp that produces ozone and emits 185 nm VUV and 254 nm UV radiation, where two radiations react with water and H_2O_2 to form hydroxyl radical ($^\bullet OH$). The photolysis of water generates $^\bullet OH$, thereby preventing the need for auxiliary chemical oxidants, such as H_2O_2, in the VUV/UV process [3,4]. Therefore, VUV/UV photodegradation is considered to be a simple and environmentally friendly water treatment technology [5]. However, some problems are found in the large-scale application of VUV/UV photoreactor in water remediation. A suitable simulation model to predict and analyze the flow field and reaction performance of the VUV/UV photoreactor is lacking. The effective modeling of

* Corresponding author.

the VUV/UV process includes the simultaneous solution of momentum, mass transfer, and radiation energy equations, and more than 40 complex kinetic schemes of reactions are found [6].

Computational fluid dynamics (CFD) is a mature and effective tool for simulating complex hydrodynamic processes and has been widely used in the design, optimization, and amplification of UV disinfection and oxidation light reactors in recent years [6,9–10]. To date, CFD simulation of H_2O_2/UV technology is relatively extensive [7–11]. Although the reaction is similar to VUV/UV, the formation mechanism of hydroxyl radical in the two reaction processes is completely different [7,11,12]. The generation of •OH radical in the VUV/UV system depends on water photodegradation at 185 nm. UV light with 185 nm wavelength is transmitted in the solution in a short distance. It plays a key role in the formation of •OH in VUV/UV AOPs, and the photolysis of hydrogen peroxide at 254 nm is the main mechanism of •OH radical generation in the H_2O_2/UV system [7].

This study aims to integrate a series of submodels, including fluid dynamics simulation, multicomponent mass transfer model, chemical reaction kinetics, and irradiance distribution in the reactor, and apply them to the airlift internal circulation photoreactor with simple structure and low-cost, so as to deeply analyze the application of VUV/UV process in water treatment. Methylene blue (MB) was studied experimentally in a continuous VUV/UV reactor and compared with the predicted results of numerical simulation. The results reveal the important hydrodynamic characteristics of VUV/UV photoreactor to provide useful suggestions for the design and optimization of VUV/UV photoreactor and promote the practical application of VUV/UV technology in water treatment.

2. Materials and methods

2.1. Hydrodynamic, mass transfer

The hydrodynamic is an important step to calculate the various species distribution in the reactor. The simulation of hydrodynamic in the reactor was performed considering a two-dimensional and unsteady state. Assuming that the fluid (water mixture) is Newtonian, incompressible, isothermal, with constant physical properties and under turbulent unsteady-state flow, the hydrodynamic and species transport equations are as follows:

Mass conservation equation:

$$\nabla \cdot (V) = 0 \tag{1}$$

Momentum conservation equation:

$$\nabla \cdot (\rho V V) = -\nabla P - \nabla \cdot \tau \tag{2}$$

where the stress tensor is:

$$\tau = \mu (\nabla V + \nabla V^T) - \frac{2}{3} \mu \nabla \cdot V U \tag{3}$$

Species conservation equation:

$$\nabla \cdot (\rho V m_i) = -\nabla \cdot J_i + R_i, \quad i = 1.2\ldots, N-1 \tag{4}$$

Where the diffusive flux of species i is estimated using Fick's first law of diffusion:

$$J_i = -D_m \nabla (\rho m_i) \tag{5}$$

In Eqs. (1)–(5), ρ, V, P and τ are fluid density, velocity vector, pressure and viscous stress tensor respectively. These equations combined with Newton's law of viscosity to the motion of the continuous fluid through computing the velocity field within the reactor. In addition, μ is molecular viscosity, m_i is the mass fraction of species i, J_i is the diffusive flux of species i, R_i is the source rate of species i (net reaction rate per unit volume) and D_m is the molecular diffusivity of species i in the mixture.

2.2. Interphase force models

There are various interchange forces such as the drag, the lift force and the added mass force during momentum exchange between the different phases. But these forces can be neglected in comparison with drag and turbulent dispersion forces [13,14]. Hence to reduce the computational complexity and time, only the drag and turbulent dispersion force was considered in this study. Accordingly, the interfacial force $\vec{F}_i$ is approximated to be the drag force and interphase turbulent dispersion force:

$$\vec{F}_i = \vec{F}_i^D + \vec{F}_i^T \tag{6}$$

where $\vec{F}_i^D$ and $\vec{F}_i^T$ are the drag force and turbulent dispersion force, respectively.

The drag force between the gas and liquid phases is calculated by the following equation:

$$\vec{F}_{lg}^D = C_{D,lg} \frac{3}{4} \frac{\rho_l \alpha_g}{d_g} |\vec{v}_g - \vec{v}_l| (\vec{v}_g - \vec{v}_l) \tag{7}$$

where C_D is the drag coefficient. The Grace relation is chosen for the drag force coefficient because bubbles are experimentally observed to be spherical and dispersed [15].

The turbulent dispersion force, $\vec{F}_i^T$, is calculated by the model of Imoberdorf and Mohseni [16]:

$$\vec{F}_i^T = C_{TD} C_D \frac{v_{tl}}{\sigma_{tl}} \left(\frac{\nabla \alpha_g}{\alpha_g} - \frac{\nabla \alpha_l}{\alpha_l} \right) \tag{8}$$

where C_{TD} is the momentum transfer coefficient for the interphase drag force, C_D is the drag coefficient as described above, v_{tl} stands for turbulent viscosity, and σ_{tl} is the liquid turbulent Schmidt number. α_g and α_l are the gas and liquid phase volume fractions respectively.

2.3. Radiative transfer model

The radiative transfer equation for an absorbing, emitting, and scattering medium at position $\vec{r}$ in the direction $\vec{s}$ is:

$$\frac{dI(\vec{r}, \vec{s})}{ds} + (a + \sigma_s) I(\vec{r}, \vec{s}) = a n^2 \frac{\sigma T^4}{\pi} + \frac{\sigma_s}{4\pi} \int_0^{4\pi} I(\vec{r}, \vec{s}') \varnothing(\vec{s}, \vec{s}') d\Omega' \tag{9}$$

where $\vec{r}$ and $\vec{s}$ are position and direction vectors, respectively. I is the radiation intensity, which depends on position and direction, n is the refractive index, σ is the Stefan–Boltzmann constant (5.67×10^{-8} Wm^{-2} K^{-4}), α is the absorption coefficient, σ_s is the scattering coefficient, Ø is the phase function, and Ω' is the solid angle. Additionally, $(a + \sigma_s)s$ is the optical thickness or opacity of the fluid (water mixture). The refractive index n is important when considering radiation in semi-transparent media [17].

2.4. Kinetic reaction model

In previous studies, detailed kinetic models for VUV systems have been studied for conditions of perfect mixing of batch scale [7,11]. In this study, 26 types of reactions occurring in the VUV/UV photoreactor (i.e., equilibrium, photochemical, and radical reactions) are summarized as shown in Table 1 with reference to the previous study.

Thus, in the presence of VUV and UV radiation, the main degradation pathways of the species are initiated by the OH radicals produced by the decomposition of water by 185 nm, leading to radical chain reactions by 185 and 254 nm.

2.5. Airlift photoreactor setup, geometry, and grid generation

A flow-through continuous operation of an airlift photoreactor was used to experimentally evaluate the CFD results. A simple 2D geometry for the airlift photoreactor with internal circulation is shown in Fig. 1. It has a conical bottom shape, is internally irradiated with a light source placed at the central core axis, and has a draft tube with internal circulation occurring around the light source. The reactor is divided into the central circulation area, bottom air, and water distribution area. It is operated with a 54 W low-pressure mercury VUV/UV lamp (customized) that

Table 1
Kinetic model of the VUV/UV photoreactor for degradation of MB

No.	Reaction equation	Rate constant	References
1	$H_2O + h\nu_{185nm} \rightarrow HO^\bullet + H^\bullet$	$\varnothing_6 = 0.330$ mol/ein	[18]
2	$H_2O + h\nu_{185nm} \rightarrow H^+ + e_{aq}^- + HO^\bullet$	$\varnothing_7 = 0.045$ mol/ein	[18]
3	$H_2O_2 + h\nu_{185nm} \rightarrow 2HO^\bullet$	$\varnothing_8 = 0.500$ mol/ein	[18]
4	$H_2O_2 + h\nu_{254nm} \rightarrow 2HO^\bullet$	$\varnothing_9 = 0.500$ mol/ein	[18]
5	$O_2 + H^\bullet \rightarrow HO_2^\bullet$	$k_1 = 2.1 \times 10^{10}$ M^{-1} s^{-1}	[18]
6	$O_2 + e_{aq}^- \rightarrow O_2^{\bullet-}$	$k_2 = 2.0 \times 10^{10}$ M^{-1} s^{-1}	[18]
7	$H_2O_2 + OH^\bullet \rightarrow HO_2^\bullet + H_2O$	$k_3 = 2.7 \times 10^7$ M^{-1} s^{-1}	[18]
8	$H_2O_2 + HO_2^\bullet \rightarrow OH^\bullet + O_2 + H_2O$	$k_4 = 5.3 \times 10^2$ M^{-1} s^{-1}	[18]
9	$H_2O_2 + O_2^{\bullet-} \rightarrow OH^\bullet + O_2 + OH^-$	$k_5 = 1.6 \times 10^1$ M^{-1} s^{-1}	[18]
10	$H_2 + OH^\bullet \rightarrow H_2O + H$	$k_6 = 6.0 \times 10^7$ M^{-1} s^{-1}	[18]
11	$OH^\bullet + OH^\bullet \rightarrow H_2O_2$	$k_7 = 4.0 \times 10^9$ M^{-1} s^{-1}	[18]
12	$HO_2^\bullet + HO_2^\bullet \rightarrow H_2O_2 + O_2 + H_2O$	$k_8 = 2.6 \times 10^6$ M^{-1} s^{-1}	[18]
13	$H^\bullet + H^\bullet \rightarrow H_2$	$k_9 = 1.0 \times 10^{10}$ M^{-1} s^{-1}	[18]
14	$OH^\bullet + H^\bullet \rightarrow H_2O$	$k_{10} = 7.0 \times 10^9$ M^{-1} s^{-1}	[18]
15	$OH^\bullet + O_2^{\bullet-} \rightarrow O_2 + HO^-$	$k_{11} = 7.0 \times 10^9$ M^{-1} s^{-1}	[19]
16	$OH^\bullet + HO_2^\bullet \rightarrow H_2O + O_2$	$k_{12} = 6.6 \times 10^9$ M^{-1} s^{-1}	[20]
17	$HO_2^\bullet + O_2^{\bullet-} \rightarrow O_2 + HO_2^-$	$k_{13} = 9.7 \times 10^7$ M^{-1} s^{-1}	[20]
18	$e_{aq}^- + OH^\bullet \rightarrow OH^-$	$k_{14} = 3.0 \times 10^{10}$ M^{-1} s^{-1}	[18]
19	$2O_2^{\bullet-} + 2H_2O \rightarrow O_2 + H_2O_2 + 2OH^-$	$k_{15} = 3.0 \times 10^{-1}$ M^{-1} s^{-1}	[18]
20	$e_{aq}^- + H^\bullet + H_2O \rightarrow H_2 + OH^-$	$k_{16} = 2.5 \times 10^{10}$ M^{-1} s^{-1}	[18]
21	$OH^\bullet + HO_2^- \rightarrow HO_2^\bullet + OH^-$	$k_{17} = 7.5 \times 10^9$ M^{-1} s^{-1}	[21]
22	$OH^\bullet + OH^- \rightarrow O^{\bullet-} + H_2O$	$k_{18} = 3.9 \times 10^8$ M^{-1} s^{-1}	[20]
23	$H^\bullet + OH^- \rightarrow e_{aq}^- + H_2O$	$k_{19} = 3.6 \times 10^8$ M^{-1} s^{-1}	[22]
24	$H_2O_2 + e_{aq}^- \rightarrow OH^\bullet + OH^-$	$k_{20} = 1.1 \times 10^{10}$ M^{-1} s^{-1}	[23]
25	$e_{aq}^- + H^+ \rightarrow H^\bullet$	$k_{21} = 2.3 \times 10^{10}$ M^{-1} s^{-1}	[23]
26	$e_{aq}^- + H_2O \rightarrow H^\bullet + OH^-$	$k_{22} = 1.9 \times 10^1$ M^{-1} s^{-1}	[23]
27	$H^\bullet + HO_2^\bullet \rightarrow H_2O_2$	$k_{23} = 1.1 \times 10^{10}$ M^{-1} s^{-1}	[23]
28	$H^\bullet + H_2O_2^\bullet \rightarrow H_2O + OH^\bullet$	$k_{24} = 9.0 \times 10^7$ M^{-1} s^{-1}	[23]
29	$e_{aq}^- + HO_2^- + H_2O \rightarrow 2OH^- + OH^\bullet$	$k_{25} = 3.5 \times 10^9$ M^{-1} s^{-1}	[24]
30	$H^\bullet + O_2^{\bullet-} \rightarrow HO_2^-$	$k_{26} = 2.0 \times 10^{10}$ M^{-1} s^{-1}	[24]
31	$OH^\bullet + MB \rightarrow Products$	$k_{27} = 6.9 \times 10^{10}$ M^{-1} s^{-1}	[20]

Fig. 1. Schematic diagram of the internal airlift circulating photoreactor for the simulation (cm).

is approximately 2.3 cm in diameter and 50 cm in length and longitudinally placed at the axial center of the reactor. In this study, the position of the draft tube was set to 0.4 of r/R, where r is the distance between the reactor wall and the draft tube, and R is the distance between the reactor wall and the light source (R) [15].

The geometry was created on ANSYS Design Modeler software. Given the characteristics of the axially symmetric structure of the reactor, the flow field simulation can be reasonably simplified with a 2D axial symmetry model. An unstructured numerical grid was implemented with a total of 14,462 elements, where the min size of the grid is 0.15 mm, and the max face size is 5.0 mm.

2.6. Initial and boundary conditions

For the initial conditions, the liquid and gas phases enter the reactor from the bottom at different flow rates. The gas and liquid phases were air and water in a standard state. A uniform air velocity Ug (0.01, 0.04, 0.07, and 0.10 m/s) was simulated for the gas inlet, and the liquid velocity was set to 0.3 m/s. The inlet MB concentration as model contaminant equaled 5 ppm. The diameter of air is 0.2 mm, the dynamic viscosity of air and water

are set to 17.9×10^{-6} Pa·s and 1.005×10^{-3} Pa·s at 20°C, respectively.

A no-slip boundary condition was imposed for the walls. Zero diffusive flux of species was specified at the walls. For radiation field boundary conditions, the lamp radiation was defined as a zero-thickness wall, semi-transparent, and non-reflecting walls. The density and viscosity of water were 998.2 kg/m³ and 1.003×10^{-3} Pa, respectively. The refractive indices of 185 and 254 nm were assigned at 1.458 and 1.376, respectively. The absorption coefficient was 35.67 (m⁻¹, UV transmittance (UVT) = 70%) and 12.78 (m⁻¹, UVT = 88%), respectively.

2.7. Numerical solution

ANSYS Fluent 16.2 was used to read the mesh and perform the CFD computations. A segregated steady-state solver was used to solve the governing equations. A second-order upwind discretization scheme was applied, except for pressure where a standard scheme was selected. The SIMPLE algorithm was chosen for the pressure–velocity coupling. The variation of velocity magnitude, model contaminant concentration, and irradiation flux at several points of the computational domain were used as indicators of convergence (at least 20 iterations). The convergence of the numerical solution was assured by monitoring the scaled residuals to a criterion of at least 10^{-4} for the MB concentration. The simulation was always tracked with time, and the solution algorithm was run under steady and transient flow simulations.

3. Results and discussion

3.1. Hydrodynamics, velocity, and holdup

The airlift photoreactor with internal circulation is powered by air, which can keep the liquid circulating in the rising and falling regions of the reactor. Fig. 2 shows the streamlined distribution of the liquid phase in the airlift photoreactor with internal circulation. The gas enters the photoreactor from the bottom inlet. In the central position of the reactor, the local liquid density is lower than the liquid outside the baffle plate and then flows upward along the surface of the light source until it reaches the reactor outlet and leaves the reactor. The liquid on the outer side of the baffle with high density is to supplement the liquid lifted up by the gas so as to flow down the reactor wall to the inlet. This repeated internal circulation flow can make the liquid in the reactor achieve a full mixing effect and provide better contact opportunities between the material components. In other words, the full mixing and contact between the various material components in the reactor liquid can receive uniform light source irradiation. This condition is conducive to the complete and effective reaction between the substances in the liquid phase.

Fig. 3 shows the radial data (Section 1 in Fig. 1) at the key position of the reactor middle height, indicating the distribution of turbulence intensity at different gas velocities. Figs. 3a and b show the contours of turbulence intensity and radial distribution data under different gas

velocity conditions. Combined with 3a and b diagrams, the intensity of turbulence in the reactor increases with the increase in gas velocity. The intensity in the rising region of the reactor is greater than that in the downflow region. The turbulence intensity in the rising region increases with

the increase in gas velocity. This condition is because the gas phase in the reactor mainly concentrates on the light source surface in the rising region. The higher the gas velocity from the bottom inlet of the reactor is, the stronger the turbulence intensity along the reactor longitudinal direction close to the light source surface. The turbulence intensity is the highest when the gas velocity at the inlet is 0.10 m/s. The large turbulence intensity can effectively make the material components in the liquid to be fully mixed and evenly irradiated by the light source. This condition greatly promotes the chemical reaction efficiency between the pollutants and oxidation free radicals in the liquid. However, the residence time of reactants in the reactor and the chance of contact with light source are reduced if the turbulence intensity is extremely high, thereby leading to a poor sewage purification effect.

Fig. 4 shows the radial data (Section 1 in Fig. 1) at the key position of the reactor middle height, representing the distribution of liquid velocity and gas holdup at different gas velocities. Figs. 4a and b show the radial distribution data of liquid velocity and gas holdup under different gas velocities. Combined with 4a and b diagrams, the liquid velocity distribution and gas holdup tend to be higher near the light source and gradually decrease to the reactor wall with the increase in gas velocity entering the reactor. This condition is due to the great force exerted on the mixture by gas injection and gas expansion at the inlet. The liquid velocity in the down-flow zone has certain velocity distribution characteristics. This condition is conducive to the internal circulation effect of the reactor and increases the circulation times of the liquid in the ascending and descending regions. This effect is the core of the airlift internal circulation reactor. However, excessive gas velocity can increase the liquid velocity and gas holdup in the reactor, which is unconducive to the residence time of reactants in the reactor. The gas holdups of 0.10 and 0.07 m/s are slightly the same, but a large difference is found compared with 0.04 m/s.
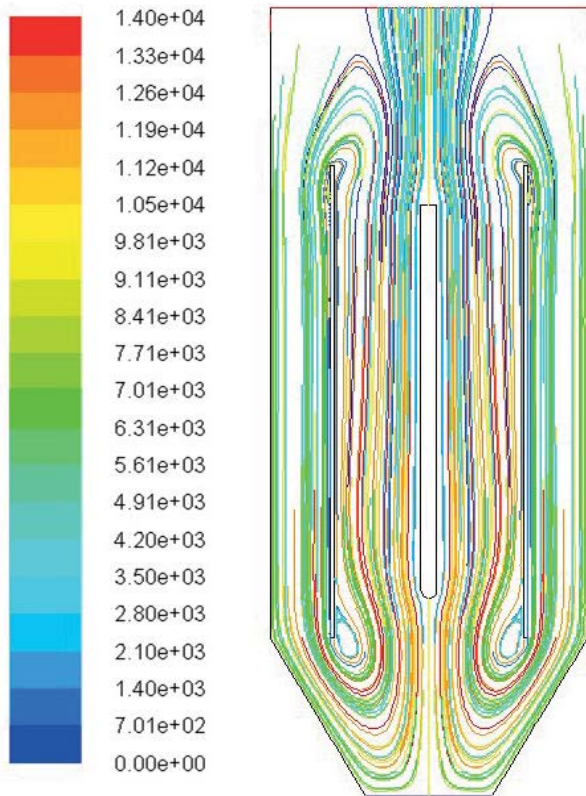
Fig. 2. Liquid-phase streamline in the vertical plane of the internal airlift circulation photoreactor.
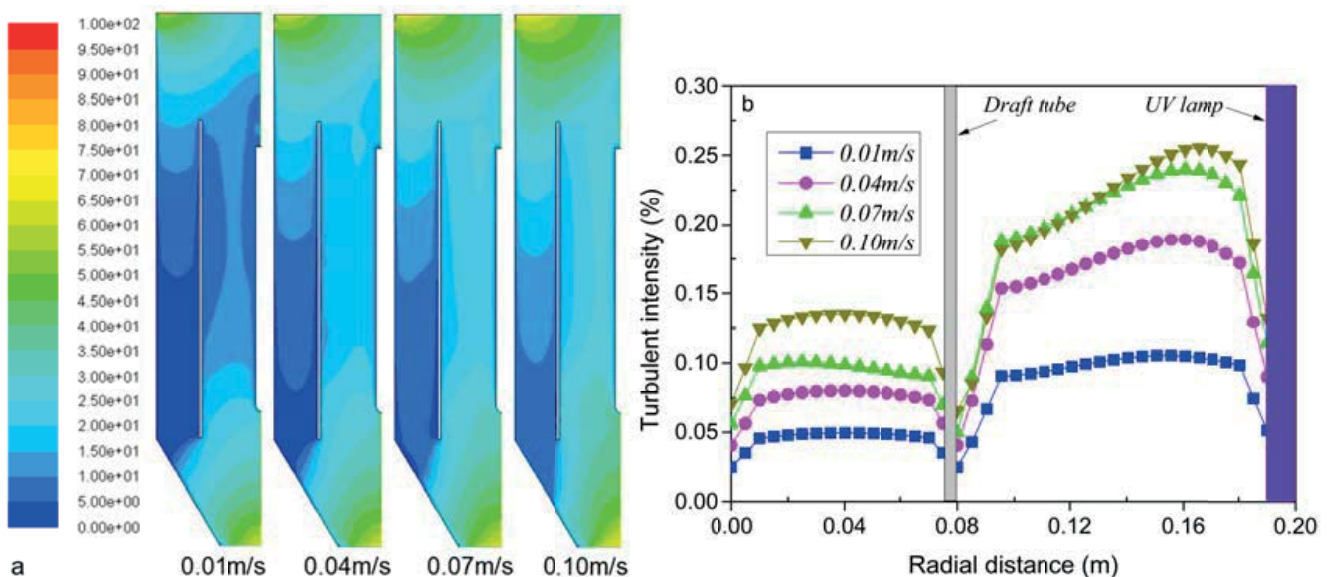
Fig. 3. The contours (a) and the radial distribution (b) of turbulent intensity at different gas inlet velocities in section 1.
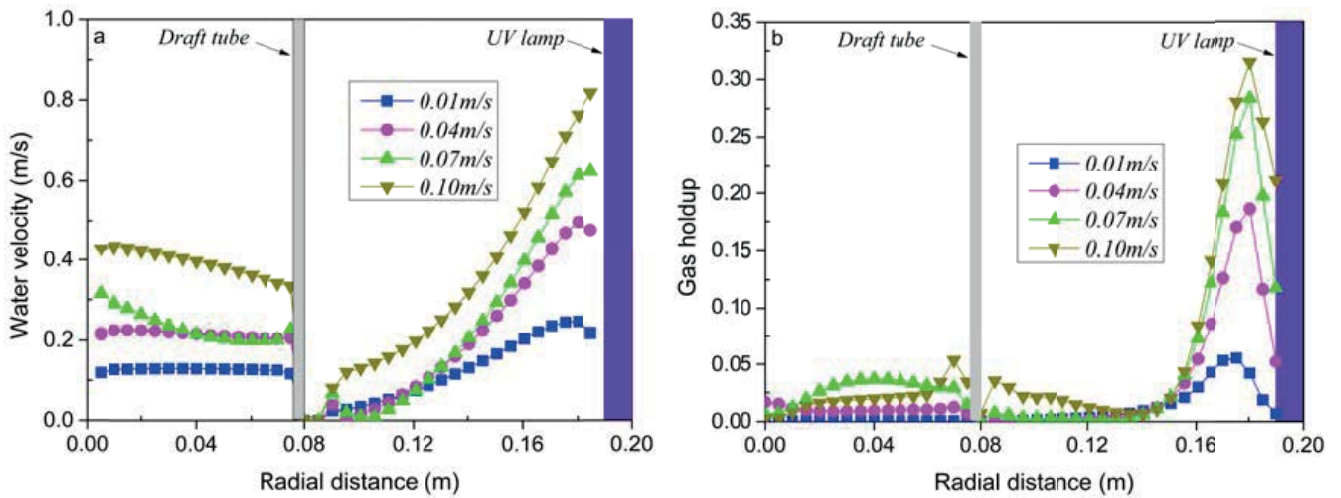
Fig. 4. The radial distribution of water velocity (a) and gas holdup (b) at different gas inlet velocities in section 1.

3.2. Radiation

All types of reactions in the photoreactor mainly depend on the energy of the light source. Thus, the location of the light source and its radiation intensity determine the degradation efficiency of pollutants. Fig. 5 shows the longitudinal distribution characteristics of the radiation intensity of the UV lamp in the photoreactor. The UV radiation intensity maps of a1 (185 nm) and a2 (254 nm) represent the UV distribution of two different wavelengths of VUV/UV light source, respectively. These wavelengths correspond to the data plots of b1 (185 nm) and b2 (254 nm), respectively. The radiation in water decreases with the increase in horizontal distance from the light source. The reaction of most reactants is intense on the wall near the light source. The baffle position in the reactor

does not obstruct the radiation area of the light source, and the liquid phase in the reactor can continue to circulate [15]. Therefore, the baffle position in the reactor and the distance between the light source are appropriate.

3.3. Chemical reaction

The degradation effect of pollutants in the airlift photoreactor with internal circulation was numerically simulated in terms of the CFD model and the kinetic process of a chemical reaction. A user-defined method was established in terms of the characteristics of water dynamics distribution in the airlift photoreactor and the response relationship between VUV/UV-MB kinetic parameters in Table 1. The chemical reaction results of numerical simulation are shown in Figs. 6 and 7. In this study, simulation in an unsteady
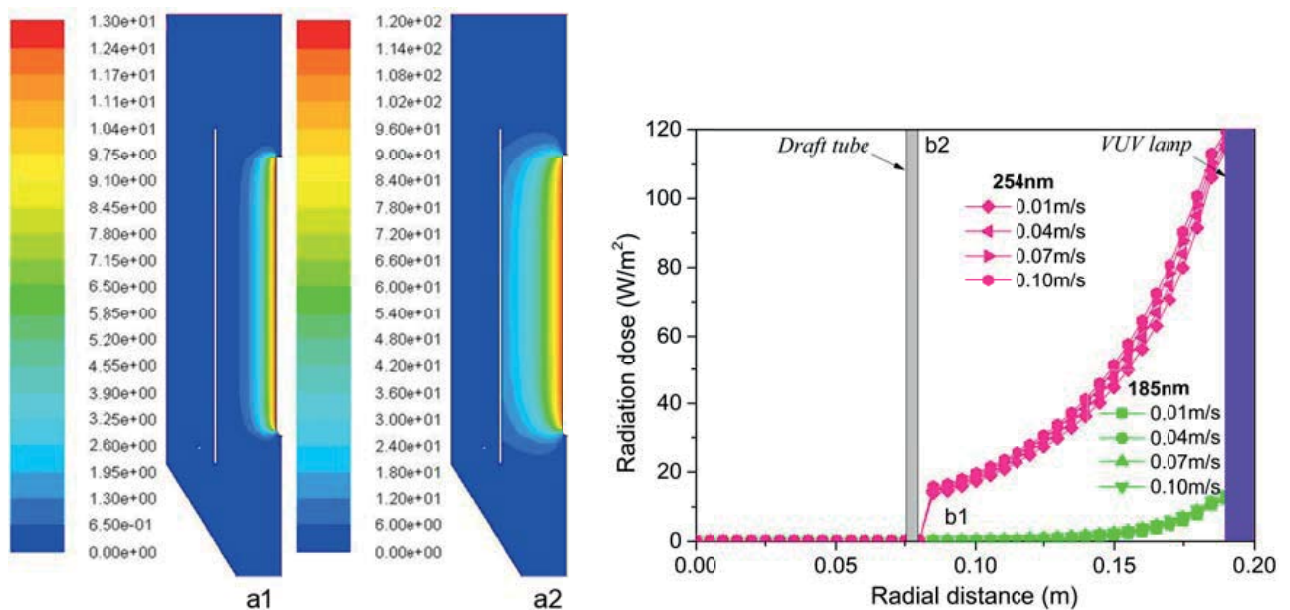
Fig. 5. Local values of ultraviolet radiation dose calculated in the whole reaction zone of photoreactor (W/m²).

environment was used to study and analyze the data after steady-state calculation. Fig. 6 shows the contours (a) and radial distribution data (b) of •OH at the reactor outlet (Section 2 in Fig. 1) at different gas velocities.

In this reaction system, the formation of hydroxyl radicals is mainly generated by VUV radiation, and the hydroxyl radical can efficiently degrade the organic pollutants in water [25]. Different from UV/H_2O_2, VUV does not need to add additional chemicals and is easy to operate; this UV-AOP has been widely investigated [26]. The distribution of hydroxyl radical concentration at different gas velocities is shown in Fig. 6. With the increase in gas velocity, the concentration of hydroxyl radicals in the rising zone of the reactor shows a decreasing trend. Many hydroxyl radicals are generated because low gas velocity drives the liquid to pass through the rising zone for a long time. From the radial distribution of the cloud image, the concentration of hydroxyl radical is higher at the distance from the light source, and the concentration decreases with the distance from the light source. This condition indicates that the reaction near the light source is strong, and many hydroxyl radicals can be generated. From the vertical distribution of the contours, the liquid water entering the reactor from the inlet is gradually irradiated by UV light to generate hydroxyl radicals. The liquid enters the reactor from the bottom of the reactor and flows out to the outlet at the top of the reactor through the tubular light source. Thus, OH radicals began to form around the light source near the entrance of the reactor and gradually increased, the highest concentration of hydroxyl radicals is found near the outlet of the reactor. When the gas velocity is 0.01 m/s, the maximum concentration reaches 3.53×10^{-2} mol/m³ (Fig. 6b), whereas the maximum concentration is 2.11×10^{-2} mol/m³ at the maximum gas velocity of 0.10 m/s. The residence time of the liquid phase in the reactor increases with the decrease in gas velocity, thereby leading to the formation of many hydroxyl radicals in the liquid phase due to VUV/UV radiation. In other words, the

185 nm UV light and water in the reactor generate hydroxyl radicals, and the hydroxyl radicals are consumed by the degradation of organic pollutants (MB) in the reaction system. Thus, they maintain a certain concentration level in the two directions of generation and consumption.

Figs. 7a and b show the data of MB concentration distribution. In this study, MB enters the reactor quantitatively from the inlet at the bottom of the reactor whether in simulation or experiment. Therefore, the MB concentration is the highest at the entrance. It is degraded by hydroxyl radicals generated by water photolysis when it passes through the ascending region and gradually decreases to the outlet. MB was reacted and degraded by OH radical, but the radial concentration distribution of Figs. 6 and 7 showed the same trend. This is because the high concentration MB near the light source is caused by the continuous rising of high concentration MB at the bottom entrance of the reactor along the light source surface. The contours and data show that the CFD numerical method can effectively simulate the distribution of pollutant concentration in the reactor. From the vertical distribution of contours, the MB concentration in the rising zone of the reactor increases gradually with the increase in gas velocity. The maximum concentration reaches 7.24×10^{-6} mol/m³ and 4.4×10^{-6} mol/m³ under the conditions of maximum and minimum gas velocity, respectively. The MB concentration in this reaction system is mainly reduced by the degradation of hydroxyl radicals. Specifically, the best degradation effect is obtained when the gas velocity is 0.01 m/s. However, extremely small gas velocity reduces the circulation speed in the reactor. With the increase in gas velocity, the internal circulation speed of liquid in the reactor is accelerated, and the chance of producing hydroxyl radicals by UV light radiation is reduced. Thus, at low gas velocity, the water molecules passing through the light source have sufficient time to be irradiated by UV light for producing hydroxyl radicals. The gas flow rate of 0.01 m/s is the best condition for water purification.
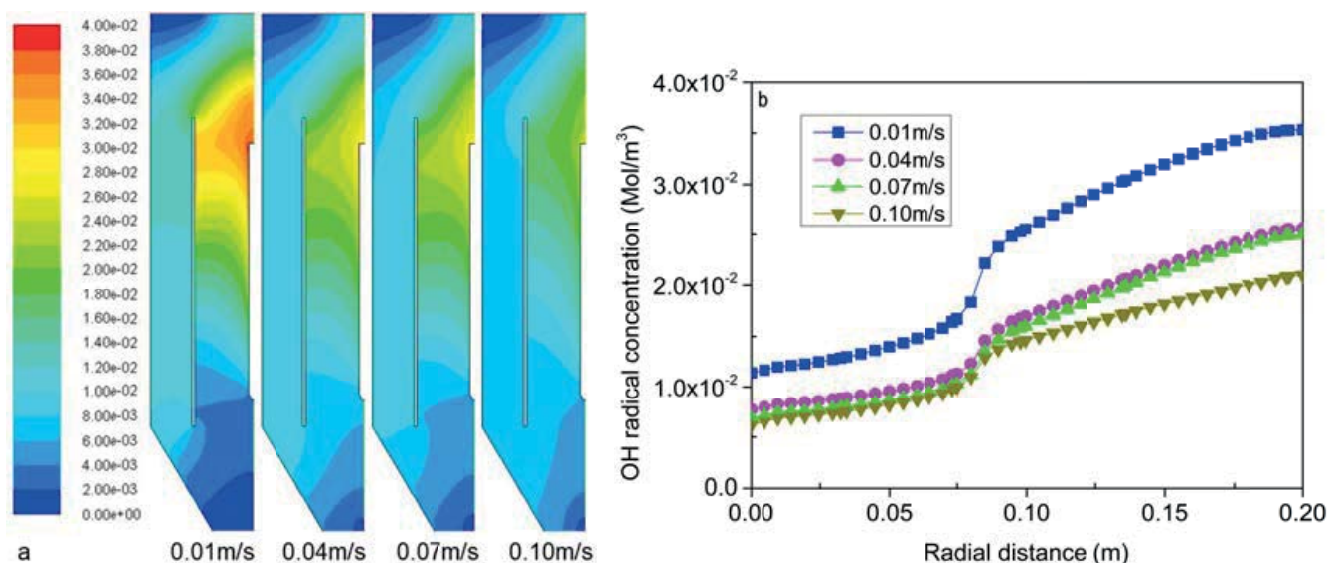
Fig. 6. The contours (a) and the radial distribution (b) of the molar concentration of OH radicals at a different gas velocity in section 2.
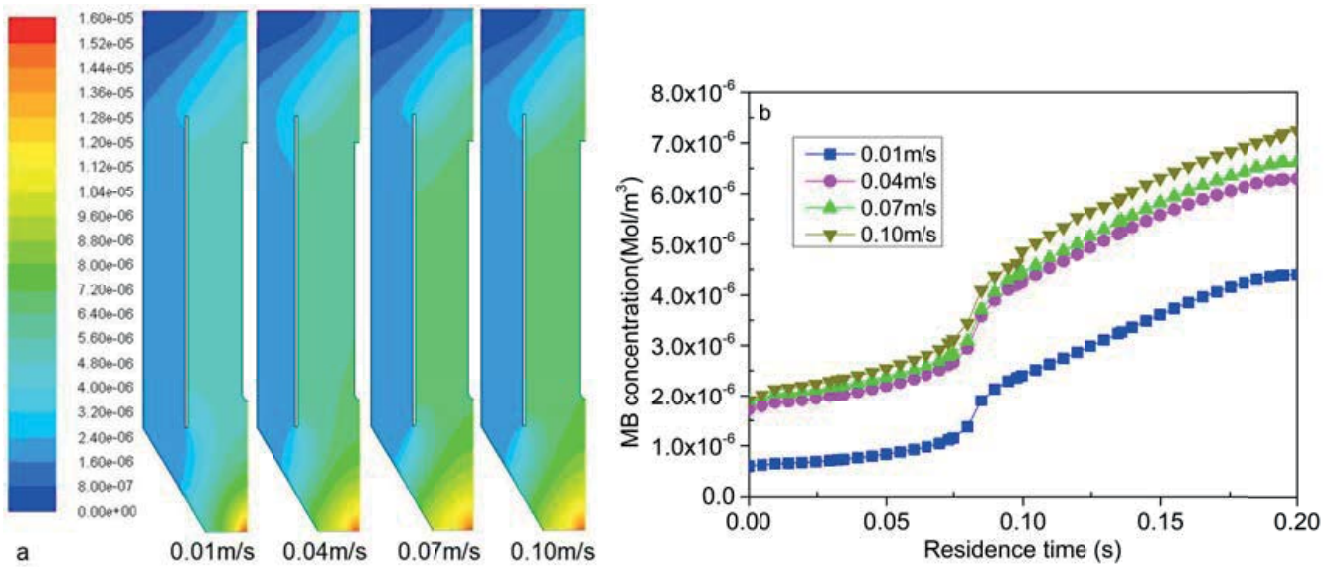
Fig. 7. The contours (a) and the radial distribution (b) of the molar concentration of MB at a different gas velocity in section 2.

3.4. Comparison of experimental and simulation results

The MB solution was treated in an airlift photoreactor with internal circulation. The comparison of the degradation effect and numerical simulation results by continuous experiment under four different gas velocity conditions is shown in Fig. 8. The degradation efficiency of MB in this study is inversely proportional to the gas velocity at the reactor inlet. At the gas velocity of 0.10 m/s, the numerical simulation results can reach 74%, and the highest removal rate in the actual experiment is approximately 59%. The structure of the reactor is reasonable and can effectively play the advantages of photocatalytic reaction and improve the degradation efficiency of MB. The experimental data are lower than the numerical prediction data, the difference range is small, and the overall prediction results are relatively good.

4. Conclusions

This study aimed to design an airlift photocatalytic reactor with internal circulation to improve the reaction performance of VUV-AOP and the degradation efficiency of the reactor. The effects of turbulence intensity, liquid velocity distribution, and gas holdup in the reactor were investigated by simulating the fluid flow characteristics and chemical reaction kinetics in the reactor. The distribution of hydroxyl radical and MB with gas velocity was analyzed and studied. The results show that the fluid flow characteristics show a certain trend with the change in gas velocity. Appropriate gas velocity increases the circulating flow effect in the reactor, but large gas velocity reduces the residence time of liquid in the reactor. Thus, the reaction cannot be conducted completely. The minimum gas velocity condition (0.01 m/s) in this study has the best degradation efficiency for MB. The results of the CFD simulation are in good agreement with the removal rate of MB in the continuous experiment. Unfortunately, there are not enough measured data (such as the concentration
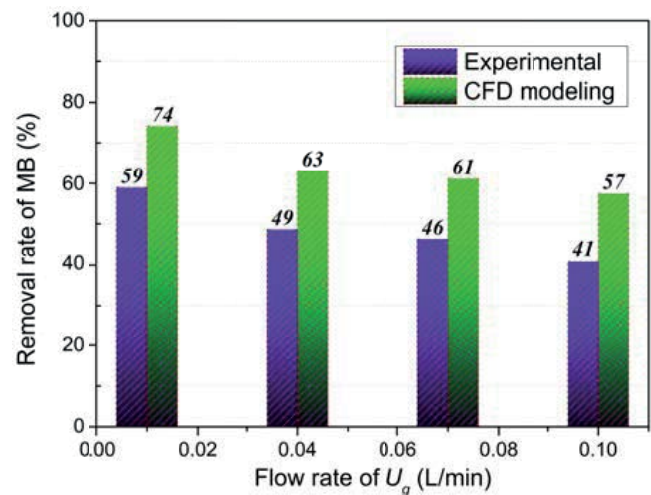
Fig. 8. Comparison of experimental data and CFD predicted results.

of free radicals, the flow characteristics in the reactor, etc.) to fully explain the distribution and variation of various physical quantities in the reactor. However, the numerical value is slightly larger because the kinetic analysis of the free radical annihilation effect of MB degradation by-product is limited. The results show that the formation of •OH radicals and the degradation efficiency of pollutants in the VUV/UV process have a strong correlation with the gas velocity entering the reactor. Therefore, these findings can serve as a reference for the establishment of a chemical reaction model for this type of reactor.

Acknowledgments

References

[1] A. Aleboyeh, M.B. Kasiri, H. Aleboyeh, Influence of dyeing auxiliaries on AB74 dye degradation by UV/H_2O_2 process, J. Environ. Manage., 113 (2012) 426–431.

[2] A. Zuorro, M. Fidaleo, M. Fidaleo, R. Lavecchia, Degradation and antibiotic activity reduction of chloramphenicol in aqueous solution by UV/H_2O_2 process, J. Environ. Manage., 133 (2014) 302–308.

[3] G. Imoberdorf, M. Mohseni, Kinetic study and modeling of the vacuum-UV photoinduced degradation of 2,4-D, Chem. Eng. J., 187 (2012) 114–122.

[4] F. Yuan, C. Hu, X.X. Hu, J.H. Qu, M. Yang, Degradation of selected pharmaceuticals in aqueous solution with UV and UV/H_2O_2, Water Res., 43 (2009) 1766–1774.

[5] K. Kutschera, H. Börnick, E. Worch, Photoinitiated oxidation of geosmin and 2-methylisoborneol by irradiation with 254 nm and 185 nm UV light, Water Res., 43 (2009) 2224–2232.

[6] K. Zoschke, N. Dietrich, H. Börnick, E. Worch, UV-based advanced oxidation processes for the treatment of odour compounds: efficiency and by-product formation, Water Res., 46 (2012) 5365–5373.

[7] U. von Gunten, Ozonation of drinking water: Part II. Disinfection and by-product formation in presence of bromide, iodide or chlorine, Water Res., 37 (2003) 1469–1487.

[8] N. Drira, R.B. Moussa, H. Mhiri, P. Bournot, H. Dhaouadi, Wastewater treatment performances and hydrodynamic of a real-scale airlift HRAP, Desal. Water Treat., 57 (2015) 15782–15791.

[9] M. Bagheri, M. Mohseni, Computational fluid dynamics (CFD) modeling of VUV/UV photoreactors for water treatment, Chem. Eng. J., 256 (2014) 51–60.

[10] M. Bagheri, M. Mohseni, A CFD-based Study of the Degradation of Micropollutants Induced by Vacuum-UV Radiation, Proceedings International Congress on Ultraviolet Technologies (IUVA), Las Vegas, NV, 2013, pp. 22–26.

[11] S.M. Alpert, D.R. Knappe, J.J. Ducoste, Modeling the UV/hydrogen peroxide advanced oxidation process using computational fluid dynamics, Water Res., 44 (2010) 1797–808.

[12] D. Gu, C. Guo, S. Hou, J. Lv, Y. Zhang, Q. Feng, Y. Zhang, J. Xu, Kinetic and mechanistic investigation on the decomposition of ketamine by UV-254 nm activated persulfate, Chem. Eng. J., 370 (2019) 19–26.

[13] J.E. Duran, M. Mohseni, F. Taghipour, Modeling of annular reactors with surface reaction using computational fluid dynamics (CFD), Chem. Eng. Sci., 65 (2010) 1201–1211.

[14] M. Luo, Q. Chen, T. Jeong, C. Jing, Numerical modelling of a three-phase internal air-lift circulating photocatalytic reactor, Water Sci. Technol., 76 (2017) 3044–3053.

[15] S. Elyasi, F. Taghipour, Simulation of UV photoreactor for degradation of chemical contaminants: model development and evaluation, Environ. Sci. Technol., 44 (2010) 2056–2063.

[16] G. Imoberdorf, M. Mohseni, Modeling and experimental evaluation of vacuum-UV photoreactors for water treatment, Chem. Eng. Sci., 66 (2011) 1159–1167.

[17] G. Mouussavi, M. Rezaei, M. Pourakbar, Comparing VUV and VUV/Fe^{2+} processes for decomposition of cloxacillin antibiotic: degradation rate and pathways, mineralization and by-product analysis, Chem. Eng. J., 332 (2018) 140–149.

[18] ANSYS, ANSYS FLUENT Theory Guide, Release 15.0, ANSYS, Inc., 2013.

[19] B.H.J. Bielski, D.E. Cabelli, R.L. Arudi, A.B. Ross, Reactivity of hydroperoxyl/superoxide radicals in aqueous solution, J. Phys. Chem. Ref. Data, 14 (1985) 1041–1100, doi: 10.1063/1.555739.

[20] G.V. Buxton, C.L. Greenstock, W.P. Helman, A.B. Ross, Critical review of rate constants for reactions of hydrated electrons, hydrogen atoms and hydroxyl radicals in aqueous solution, J. Phys. Chem. Ref. Data, 513 (1988) 2315–2328.

[21] J.C. Crittenden, S. Hu, D.W. Hand, S.A. Green, A kinetic model for H_2O_2/UV process in a completely mixed batch reactor, Water Res., 33 (1999) 2315–2328.

[22] Z.D. Draganic, I.G. Draganic, Studies on the formation of primary yields of hydroxyl radical and hydrated electron in the g-radiolysis of water, J. Phys. Chem., 75 (1971) 765–772.

[23] A.A. Basfar, H.M. Khan, A.A. Al-Shahrani, W.J. Cooper, Radiation induced decomposition of methyl *tert*-butyl ether in water in presence of chloroform: kinetic modelling, Water Res., 39 (2005) 2085–2095.

[24] F.T. Mak, S.R. Zele, W.J. Cooper, C.N. Kurucz, T.D. Waite, M.G. Nickelsen, Kinetic modeling of carbon tetrachloride, chloroform and methylene chloride removal from aqueous solution using the electron beam process, Water Res., 31 (1997) 219–228.

[25] N.V. Klassen, D. Marchington, H.C.E. McGowan, H_2O_2 determination by the I_3^- method and by $KMnO_4$ titration, Anal. Chem., 66 (1994) 2921–2925.

[26] B.A. Wols, D.J.H. Harmsen, J. Wanders-Dijk, E.F. Beerendonk, C.H.M. Hofman-Caris, Degradation of pharmaceuticals in UV (LP)/H_2O_2 reactors simulated by means of kinetic modeling and computational fluid dynamics (CFD), Water Res., 75 (2015) 11–24.